Shape-Controlled Synthesis of Cobalt-based Nanocubes, Nanodiscs, and Nanoflowers and Their Comparative Lithium-Storage Properties

Jun Song Chen,[†] Ting Zhu,[†] Qiu Hong Hu,[‡] Junjie Gao,[§] Fabing Su,[§] Shi Zhang Qiao,*,[‡] and Xiong Wen Lou*,[†]

School of Chemical and Biomedical Engineering, Nanyang Technological University, 70 Nanyang Drive, Singapore 637457, Singapore, ARC Centre of Excellence for Functional Nanomaterials, The University of Queensland, Level 5W, AIBN (Building 75), Brisbane, Queensland 4072, Australia, and State Key Laboratory of Multiphase Complex System, Institute of Process Engineering, Chinese Academy of Sciences, Beijing, China 100190

ABSTRACT Facile hydrothermal methods have been developed to synthesize large Co_3O_4 nanocubes, β-$Co(OH)_2$ hexagonal nanodiscs and nanoflowers. Samples are thoroughly characterized by field-emission scanning electron microscopy, transmission electron microscopy, X-ray diffraction, Brunauer−Emmett−Teller method, and thermogravimetric analysis. The Co_3O_4 nanocubes have an average size of about 350 nm with a perfect cubic shape, and the β-$Co(OH)_2$ nanodiscs are uniform hexagonal platelets, whereas the β-$Co(OH)_2$ nanoflowers are assembled from large sheetlike subunits. After thermal annealing in air at a moderate temperature, the as-prepared β-$Co(OH)_2$ samples can be converted into spinel Co_3O_4 without significant alterations in morphology. We have also investigated the comparative lithium storage properties of these three Co_3O_4 samples with distinct morphologies. The nanoflower sample shows highly reversible lithium storage capability after 100 charge−discharge cycles.

KEYWORDS: cobalt-based • nanocube • nanodiscs • nanoflower • lithium-ion batteries

INTRODUCTION

As an important p-type semiconductor, cobalt oxide (Co_3O_4 in particular) has gained increasing attention because of its applications in many fields, such as gas sensing, catalysis, and lithium-ion batteries (1−13). With a well-known spinel crystal structure, Co_3O_4 has a cubic close packing array of O atoms, where the tetrahedral 8a sites and the octahedral 16d sites are occupied by Co(II) and Co(III) ions, respectively (14). One of the widely practiced methods to obtain nanostructured Co_3O_4 is via thermal decomposition of the precursor crystals such as cobalt hydroxide ($Co(OH)_2$) and carbonate ($CoCO_3$) because morphology control of these precursor crystals is less challenging (15, 16). β-$Co(OH)_2$, which has an anisotropic layered hexagonal crystal structure, can be synthesized in the shapes of one-dimensional (1D) nanorods and two-dimensional (2D) nanodiscs. For example, we recently synthesized β-$Co(OH)_2$ nanoneedles and observed an interesting topotactic transformation to Co_3O_4 nanotubes by slow oxidation in solution (3). These β-$Co(OH)_2$ nanoneedles can also be converted to single-crystalline mesoporous Co_3O_4 nanoneedles by thermal decomposition in air at 200−400 °C (17). Both these two materials have found promising applications in different

fields: β-$Co(OH)_2$ is quite electrochemically active to serve as a good electrode material for supercapacitor (18, 19), whereas Co_3O_4 is widely studied in lithium-ion batteries (8, 17, 20, 21) as well as catalysis (4, 13). As summarized in a recent review article (13), Co_3O_4 has been engineered into zero-dimensional (0D) nanoparticles (22), 1D structures such as nanowires (2, 11, 12, 23−26), nanorods (4, 17, 27), nanotubes (10, 17, 28, 29), 2D nanodiscs, nanosheets, or nanoplatelets (30−34), three-dimensional (3D) nanocubes (5, 35−37), and even hierarchical nanoflowers or more complex structures (6, 38−43).

Among all the Co_3O_4 nanostructures, nanocubes have attracted remarkable research interests, because they are perfect representation of the cubic crystal strcuture of Co_3O_4 with dominantly exposed (001) crystal planes, which is of importance for studying of crystal facet dependent properties, e.g., activity and selectivity in catalysis (4, 5). Until now, there are several reported methods for synthesis of Co_3O_4 nanocubes (5, 22, 35, 36, 44, 45). However, the size of those nanocubes obtained is generally in the range of 5−50 nm. Even though it is claimed that the nanocubes can be synthesized with controllable sizes ranging from 10 to 100 nm by varying experimental parameters like reaction temperature or time (35), synthesis of well-defined Co_3O_4 nanocubes larger than 100 nm still remains challenging. Herein, we report a poly(vinylpyrrolidone)(PVP)-mediated hydrothermal method to synthesize perfect Co_3O_4 nanocubes (designated as sample I) with an average edge length of about 350 nm. Such large Co_3O_4 nanocubes have not been synthesized before, and they may be promising candidates for different
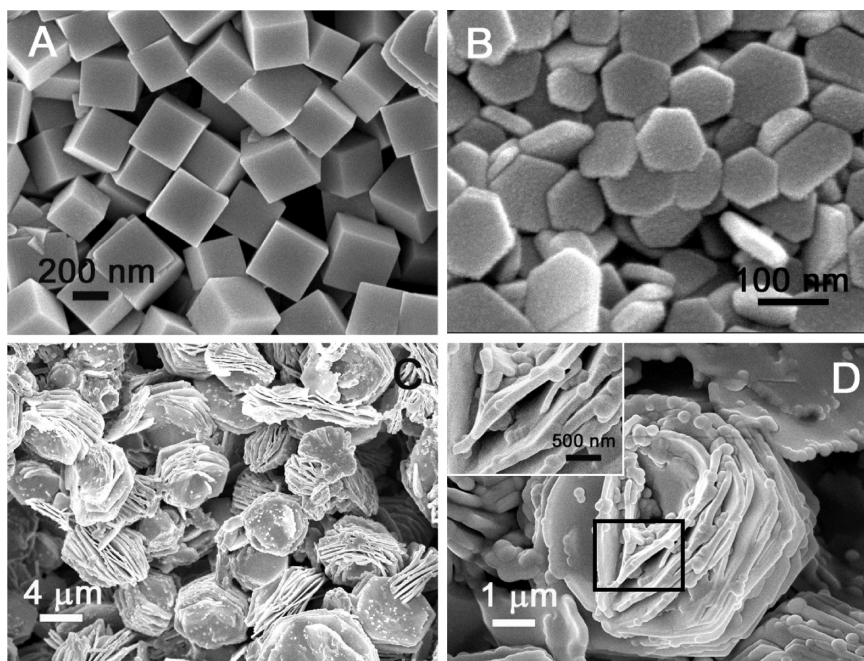
FIGURE 1. Field-emission scanning electron microscopy (FESEM) images of (A) sample I, (B) sample II, and (C, D) sample III before calcination. The inset in D shows the magnified image of the region marked by the black square.

applications, such as serving as model systems to study the crystal growth of Co_3O_4 with exposed (001) planes and their shape-dependent properties. The versatility of our system is further demonstrated by producing uniform β-$Co(OH)_2$ hexagonal nanodiscs (designated as sample II) and nanoflowers (designated as sample III) through variation of experimental parameters. All the as-synthesized samples can be easily converted to pure Co_3O_4 samples by thermal annealing without significant alterations in morphology.

As a transition metal oxide, Co_3O_4, together with other spinel materials (46), has been intensively studied as potential high-capacity anode materials for lithium-ion batteries (1, 8, 9, 20, 21, 43, 47−53). This category of anode materials assumes a distinct lithium storage mechanism based on conversion reactions: $MO + 2Li^+ + 2e^- \leftrightarrow Li_2O + M$ (M = Fe, Co, Ni, etc.) (54). The uptake and removal of lithium are realized through the formation and decomposition of a Li_2O matrix (55). Co_3O_4 is particularly attractive in this area because Co_3O_4 can uptake more than 8 lithium per formula unit with a reversible capacity as high as 1000 mA h g^{-1} (9), which is more than three times of that of commercial graphitic anodes (<370 mA h g^{-1}). However, the major drawbacks of quick capacity fading upon extended cycling and/or poor rate capability (28) hinder the practical use of Co_3O_4. These problems could in part originate from the large volume change during lithium insertion/deinsertion, which leads to disintegration of the material and loss of electrical contact, eventually causes failure of the electrode. Another contributing factor could be the formation of a solid-electrolyte interface (SEI), which usually results from side reactions such as reductive decomposition of the electrolyte (20). Thus, generating Co_3O_4-based anode materials with long-term stable cycle life is of great challenge. Furthermore, most reports in this area study only the lithium storage properties of one type of Co_3O_4 nanostructure

(2, 10−12, 17, 28), and there has been very few reports studying the comparative lithium storage properties of different Co_3O_4 nanostructures. To this end, we further investigate the electrochemical properties of three as-obtained Co_3O_4 samples with distinct structures as potential anode materials for lithium-ion batteries. In particular, the Co_3O_4 nanoflower sample with a 3D hierarchical structure demonstrates best performance with enhanced capacity retention after prolonged charge−discharge cycling up to 100 cycles.

RESULTS AND DISCUSSION

The morphologies of the uncalcined samples are first examined by FESEM, with the results shown in Figure 1. As depicted in Figure 1A, sample I consists mainly of nanocubes with an average size of about 350 nm and bounded by relatively smooth surfaces. The nanocubes are observed to have a perfect cubic shape with sharp corners and edges. It has been proposed that the formation of such Co_3O_4 nanocubes with the presence of nonionic surfactant (PVP in this case) might follow an "oriented attachment" mechanism (44). In such a process, nanocubes with smaller dimensions are first formed under the current hydrothermal conditions. The polymer surfactant will then adsorb on the surface of these nanocubes to prevent them from irregular agglomeration. After prolonged reaction, these small nanocubes will attach to neighboring ones on which the surface is less covered by the surfactant (44), thus giving rise to much larger nanocubes.

The nanodiscs in sample II are shown in Figure 1B. These nanodiscs are well-defined hexagonal platelets with smooth surface reflecting the hexagonal crystal structure of β-$Co(OH)_2$. These nanodiscs are about 50 nm in size and 10−20 nm in thickness. It was suggested that the presence of PVP is crucial to the formation of such platelet-like
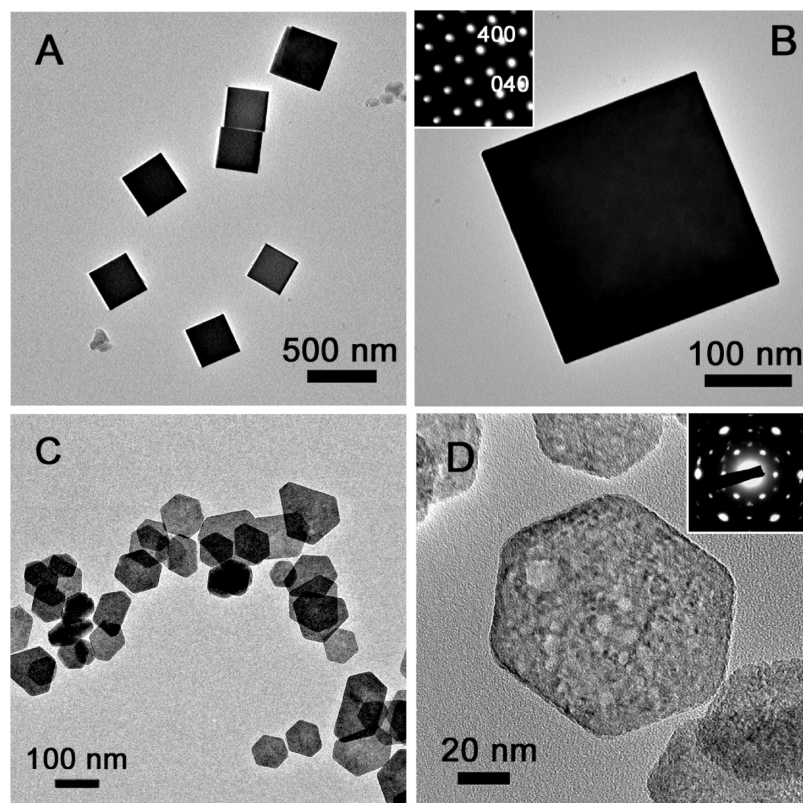
FIGURE 2. Transmission electron microscopy (TEM) images of (A, B) sample I and (C, D) sample II. The insets in B and D are the selected-area electron diffraction (SAED) patterns of the corresponding sample before calcination.

structure (30). The addition of a relatively large amount of PVP (1.2 g, see experimental section) into the reaction system creates a quite viscous environment which allows slow nucleation of the precursor. Soon after the platelet-like structure is formed, the PVP quickly adsorb on its surface, preventing it from stacking along the [001] direction to produce one-dimensional structure (28). As a result, the subsequent crystal growth is only allowed in the lateral directions, leading to the final structure of hexagonal nanodiscs.

Images C and D in Figure 1 illustrate the morphology of sample III, which is observed to consist of interesting flower-like structures. The high-magnification image (Figure 1D) reveals that these nanoflowers, about 6 μm in diameter, are composed of sheet-like subunits with a thickness of about 100 nm (Figure 1D, inset). The cosolvent PEG400 plays a pivotal role in the formation of these flower-like β-Co(OH)$_2$ microstructures. Specifically, it is known that PEG400 will form complexes with Co^{2+} in the solution (56) and thus retarding the movement of the cations, resulting in a slow generation of β-Co(OH)$_2$. Such a process is probably facilitated by the PVP micelles formed in the reaction medium. At the same time, this interaction may probably favor the intergrowth of β-Co(OH)$_2$ platelets, leading to the hierarchical 3D architecture of the product (38). It is also discussed that the concentration of Co(NO$_3$)$_2$ precursor is crucial in determining the final structure of the nanoflower. With a particular concentration (25 mM in this case), there is just suitable amount of nuclei in the reaction solution, which allows fast anisotropic growth of crystals, leading to the formation of a curved structure (6). The subsequent layer-by-layer stacking of these curved structures gives rise to the hierarchical flower-like structure.

The samples are further examined using TEM, as shown in Figure 2. Figure 2A shows a few free-standing nanocubes on their (001) faces. Consistent with the above FESEM observation, these cube-like crystals are well faceted. The (001) plane is then viewed at a higher magnification (Figure 2B), which shows a perfect square. The selected-area electron diffraction (SAED; Figure 2B, inset) pattern of this single-crystal cube exhibits a 4-fold symmetry confirming the [001] zone axis. Figure 2C shows many nanodiscs with a relatively narrow size distribution. A single nanodisc is displayed at a higher magnification in Figure 2D, which gives a well-defined hexagonal shape. The surface roughness observed could be caused by the irritation of the high-energy electron beam because metal hydroxides especially in the form of nano-platelet are quite unstable. The electron beam with very high energy can easily cause the material to decompose, thus leaving defects or holes in the structure. The SAED pattern (Figure 2D, inset) proves that these β-Co(OH)$_2$ nanodiscs are single-crystalline and have a hexagonal structure lying on the (001) planes.

The crystal phases of the as-prepared samples are confirmed by XRD (Figure 3). Sample I has mixed phases of both spinel Co$_3$O$_4$ (JCPDS card no. 42−1467, S.G.: $Fd3m$, $a_o =$ 8.0837 Å), and hexagonal β-Co(OH)$_2$ (JCPDS card no. 30−0443, S.G.: $P\bar{3}$ $m1$, $a_o =$ 3.1830 Å, $c_o =$ 4.6520 Å), whereas the other two samples contain almost pure hexagonal β-Co(OH)$_2$. The peak intensities of the nanocubes are

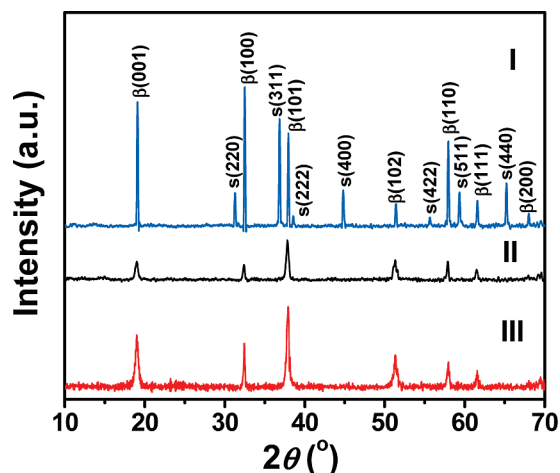**FIGURE 3. X-ray diffraction (XRD) patterns of sample I, II, and III. β, β-Co(OH)$_2$; s, spinel Co$_3$O$_4$.**
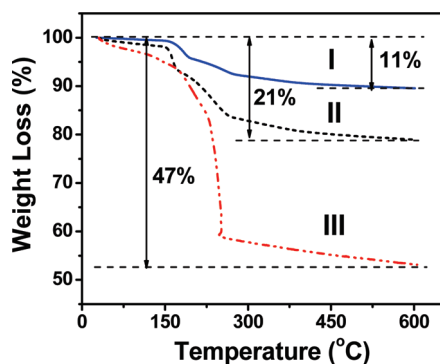

FIGURE 4. Thermogravimetric analysis (TGA) curves of sample I, II, and III.

generally higher than that of the other two samples, indicating larger crystallites in sample I, which is consistent with above morphological observations.

β-Co(OH)$_2$ can be readily converted into pure Co$_3$O$_4$ by thermal treatment based on the following reaction: $6Co(OH)_2$ (s) + O$_2$ (g) → 2Co$_3$O$_4$ (s) + 6H$_2$O (g) (34). For example, Liu et al. (31) have shown that if the calcination temperature is increased to 600 °C, holes will be created at the center of these β-Co(OH)$_2$ nanodiscs, giving rise to ringlike Co$_3$O$_4$. To find the appropriate annealing temperature for the thermal treatment, we performed thermogravimetric analysis (TGA) for all samples, with the results given in Figure 4. In agreement with the above XRD data, sample I exhibits a weight loss of about 11 %, suggesting that there is still a small fraction of β-Co(OH)$_2$ and possible organic species present in the product. The weight loss of sample II is about 21 %, which is higher than the calculated value of 13.6 % corresponding to β-Co(OH)$_2$ → Co$_3$O$_4$ (17). This is likely due to the combustion of adsorbed organic species, considering that relatively large amount of organic capping agent PVP is used in the synthetic system (see Experimental Section). Sample III gives the highest weight loss of 47 %, which is conceivable as PEG400 is used as the cosolvent with 50 vol % in the reaction medium (see Experimental Section).

On the basis of the above TGA data, the weight loss mainly takes place at about 280 °C. Thus, all three samples were calcined at 300 °C in air to obtain pure Co$_3$O$_4$. Figure

5A shows XRD patterns of the samples after calcination. Obviously, the samples have been completely transformed into pure spinel Co$_3$O$_4$ (JCPDS card no. 42−1467). The morphologies of the heat-treated samples were then examined by FESEM and TEM. No apparent alterations can be observed for sample I, which still shows a perfect cube-like shape (Figure 5B). Sample II also demonstrates good thermal stability as the hexagonal platelet structure can be retained (Figure 5C). There are, however, some noticeable changes after calcination, as the surface of the nanodiscs becomes substantially rougher. From the TEM image (Figure 5D), these surface defects can be more clearly identified as a porous structure resulting from the thermal decomposition (17). The formation of such defects can be probably attributed to the recrystallization process during calcination, where the small nanocrystals grow into an interconnected porous structure with large pores (17). The SAED pattern (Figure 5D, inset) reveals that a hexagonal spot pattern is still visible. This indicates the relatively poor single-crystallinity of these nanodiscs and confirms the topotactic transformation from (001) planes of β-Co(OH)$_2$ to (111) planes of Co$_3$O$_4$ (3). Sample III is also shown to be quite thermally stable, as no apparent collapse of flowerlike structure can be observed (Figure 5E). It is interesting to observe that the nanosheets that form the nanoflowers become much thinner after calcination (Figure 5F, inset). This can be understood from the above TGA result that sample III contains large amount of organic contents.

The surface area of the calcined samples was measured using the Brunauer−Emmett−Teller (BET) method. The N$_2$ adsorption−desorption isotherms at 77 K are shown in Figure 6, with the insets showing the pore size distribution by the Barrett−Joyner−Halenda (BJH) method. The isotherm of sample I (Figure 6A) can be classified to be a type IV isotherm with a type H3 hysteresis loop at the relative pressure of 0.4 − 0.7, which indicates a mesoporous structure and gives rise to a relatively high BET specific surface area of 91.4 m^2 g^{-1}, and a total pore volume of 0.149 cm^3 g^{-1} (57). Sample II shows a type III isotherm without a distinct hysteresis loop (Figure 6B), which suggests the absence of a mesoporous structure and leads to a slightly lower BET specific surface area of 76.8 m^2 g^{-1}. Interestingly, sample II gives a much higher total pore volume of 0.312 cm^3 g^{-1}. Sample III exhibits a type III isotherm with a type H3 hysteresis (Figure 6C), which reveals its mesoporous characteristics and leads to a BET specific surface area of 66.5 m^2 g^{-1} and a total pore volume of 0.147 cm^3 g^{-1}. Moreover, a striking peak around 4−4.5 nm can be observed in the pore size distribution calculated from the desorption branch of all three samples (the insets in Figure 6). Such a peak could be an artifact corresponding to capillary evaporation at the lower end of the hysteresis loop with a relative pressure of about 0.4 − 0.5 (55, 58).

Figure 7A shows the first cycle charge−discharge voltage profiles of the three samples after calcination. The voltage profiles are generally consistent with previous studies (2, 11, 12). During the first discharge, there is a distinct
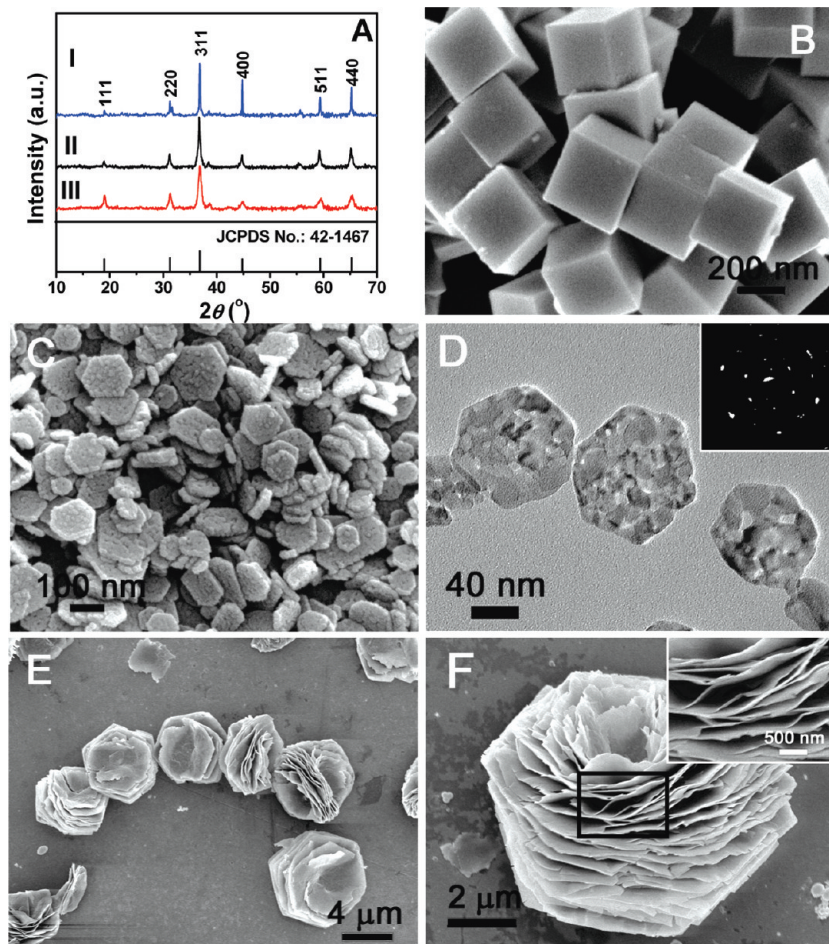
FIGURE 5. (A) XRD patterns of sample I, II and III after calcination at 300 °C in air. The standard pattern is shown at the bottom of the figure. (B) FESEM of sample I, (C) FESEM and (D) TEM images image of sample II, and (E, F) FESEM images of sample III after calcinations at 300 °C in air. The inset in D shows the SAED pattern of sample II, and the inset in F shows the magnified image of the region marked by the black square.

voltage plateau at about 1.0 V, followed by a gradual decay. As a result, a high discharge capacity of 1250 mA h g^{-1} to 1350 mA h g^{-1} is observed. These discharge capacities are much higher than the theoretical capacity of Co_3O_4, and this could be attributed to irreversible reactions, such as decomposition of electrolyte (28). The first charge capacity is about 900 mA h g^{-1}, leading to an irreversible capacity loss of about 30 % in all three samples. This large initial loss could be considered as the nature of the conversion reaction based mechanism (11), and it is also believed to be caused by the formation of the SEI on the surface of the electrode material (59).

Figure 7B depicts the cycling performance of the three samples up to 100 cycles. It is apparent that sample II shows the highest capacity of more than 1200 mA h g^{-1} in the course of first few cycles, which is higher than that of 1D Co_3O_4 nanoneedles and mesoporous nanotubes previously reported (17, 28). This is probably because of its highly rough surface and porosity which provide more active sites during charging-discharging processes, and its small thickness granting a short diffusion path for more efficient lithium diffusion. However, sample II suffers from rapid capacity fading thereafter. This could be caused by aggregation of nanodiscs during prolonged cycling in view of its relatively

small particle size, leading to quick diminishment of active surface area. Sample III delivers a lower capacity of about 1000 mA h g^{-1}. Both these two samples demonstrate a general trend of increase in capacity during the first 10 cycles of the measurement, which has also been observed in other literatures (11, 12, 20). One possible reason for the observation of a capacity which is higher than the theoretical value (890 mA h^{-1}) is that there exist many other side reactions, e.g., decomposition of electrolyte, during the charge—discharge process. Apparently, sample III shows a much better cyclic retention compared to sample II. A reversible capacity of as high as 694 mA h g^{-1} can still be retained after 100 cycles, which should be considered advantageous compared to other reported Co-based anodes tested under similar conditions (21, 52, 53). This is conceivable as the unique 3D hierarchical structure of the nanoflowers provides long-term structural stability against the volume change during the charge—discharge process (60). Surprisingly, even though sample I has the highest specific area of 91.4 m^2 g^{-1}, it gives the lowest capacity of 700 mA h g^{-1}. This might be attributed to its relatively large effective particle size that leads to more severe local volume alterations during the charge—discharge process. Nevertheless, at the end of 100
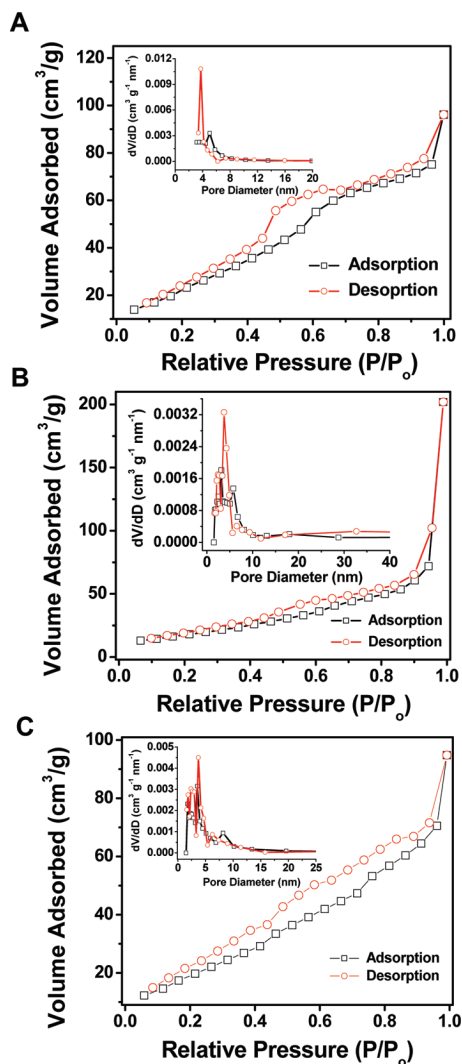
FIGURE 6. N₂ adsorption–desorption isotherms of the samples after calcinations at 300 °C: (A) sample I, (B) sample II, and (C) sample III. The inset shows the pore size distribution of the corresponding sample.

cycles, all three samples are still able to deliver a capacity that is higher than that of commercialized graphite.

CONCLUSIONS

In summary, a PVP-mediated hydrothermal method has been developed to synthesize Co_3O_4 nanocrystals with a perfect cubic shape. These as-prepared nanocubes have an average length of about 350 nm. To the best of our knowledge, Co_3O_4 nanocubes above 100 nm in size have not been synthesized before. By varying the experimental parameters, β-$Co(OH)_2$ hexagonal nanodiscs, as well as hierarchical nanoflowers built from β-$Co(OH)_2$ nanosheets, can be readily synthesized. After calcinations in air at a moderate temperature (300 °C), all three as-synthesized samples can be converted to spinel Co_3O_4 without significant alterations in shape. The three as-obtained Co_3O_4 samples with different shapes have been characterized for their potential use as anode materials in lithium-ion batteries. The electrochemical measurements show that the nanoflower sample exhibits the best performance with quite reversible capacities (649
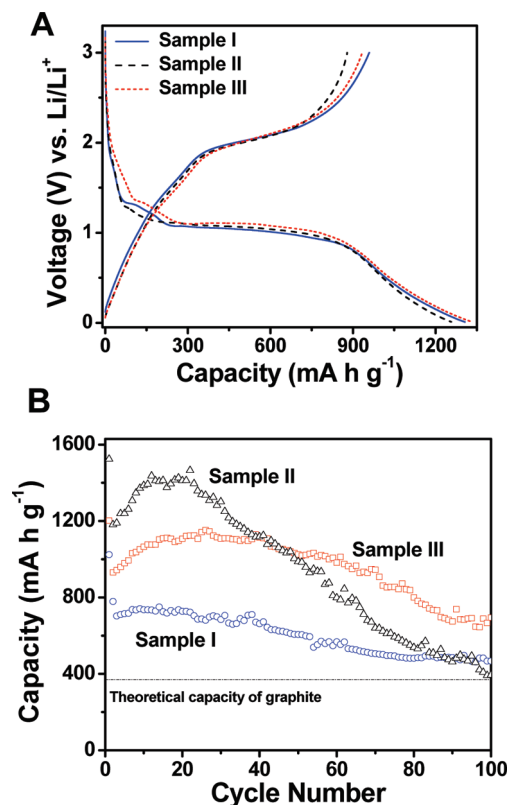

FIGURE 7. (A) First-cycle charge–discharge voltage profiles of the three calcined samples at a current rate of 50 mA g⁻¹ between 10 mV and 3 V. (B) Cycling performance of the samples at 100 mA g⁻¹ with the same voltage window.

mA h g⁻¹ after 100 cycles). This study should provide more insights about the effect of structures on the electrochemical lithium storage properties of metal oxide nanomaterials. Study of the structural effect on magnetic properties of these Co_3O_4 nanostructured materials should also be interesting.

EXPERIMENTAL SECTION

Material Preparation. *Synthesis of Nanocubes.* In a typical synthesis, 25 mL of ammonia solution (28–30%, Reagent Chemicals) was first mixed with ultra pure water (1/1, v/v). Then, 0.05 g of poly(vinylpyrrolidone) (PVP; M.W. = 58,000, Reagent Chemicals) was dissolved in the solution. After shaking for a few minutes, 0.364 g of cobalt nitrate hexahydrate ($Co(NO_3)_2 \cdot 6H_2O$, 98+%, Sigma Aldrich) was added into the reaction medium to reach a concentration of 25 mM. After sonication, a browny transparent solution was obtained, which was then transferred into a 60 mL Teflon-lined stainless steel autoclave. The autoclave was kept in an electric oven at 180 °C for 6 h, after which the autoclave was taken out and cooled naturally to room temperature. After that, the black precipitate was harvested and washed with ultra pure water several times via centrifugation. The product was then dried at 60 °C overnight, before being calcined at 300 °C for 2 h in air to be converted into Co_3O_4.

Synthesis of Hexagonal Nanodiscs. In a typical synthesis, 1.5 mL of 1.0 M cobalt acetate tetrahydrate (($CH_3COO)_2Co \cdot 4H_2O$, reagent grade, Sigma Aldrich) was added into 55.5 mL of ultra pure water under vigorous stirring. 1.2 g of PVP (M.W. = 10,000, Sigma Aldrich) was then added into the solution. After the PVP is fully dissolved, 3 mL of 1.0 M NaOH solution was added into the medium. Part of the mixture was transferred into a 60 mL Teflon-lined

stainless steel autoclave with only 80% of volume filled, which was then kept in an electric oven at 180 °C for 24 h. After the autoclave was cooled down to room temperature, the precipitate was collected and washed with ultra pure water several times via centrifugation, before the product was dried at 60 °C overnight. The product was then calcined at 300 °C for 2 h in air.

Synthesis of Nanoflowers. In a typical synthesis, 25 mL of poly(ethylene glycol)−400 (PEG400, Reagent Chemicals) was mixed with ammonia (28−30%) (1/1; v/v). Then, 0.05 g of PVP (M.W. = 58 000, Reagent Chemicals) was dissolved in the solution. After shaking for a few minutes, 0.364 g of $Co(NO_3)_2 \cdot 6H_2O$ was added into the reaction medium to reach a concentration of 25 mM. After sonication, a pink transparent solution was obtained, which was then transferred into a 60 mL Teflon-lined stainless autoclave. The autoclave was kept in an electric oven at 180 °C for 3 h, after which it was taken out and cooled down to room temperature. After that, the pink precipitate was harvested and washed with ultra pure water several times via centrifugation. The product was then dried at 60 °C overnight, before being calcined at 300 °C for 2 h in air.

Material Characterizations. The structure and morphology of products were examined with transmission electron microscopy (TEM; JEOL, JEM-2010, 200 kV), and field-emission scanning electron microscopy (FESEM; JEOL, JSM-6700F, 5 kV). The powder X-ray diffraction (XRD) analysis was carried out with a Bruker D8 - Advance X-ray Diffractometer (Cu Kα radiation, λ = 1.5406 Å), from 10 to 70° at a scan rate of 0.01 °/s. The N_2 adsorption and desorption isotherm was obtained at 77 K using Quantachrome Instruments, Autosorb AS-6B. The BET surface area was estimated using adsorption data in a relative pressure ranging from 0.05 to 0.3. The thermogravimetric analysis (TGA) was performed from room temperature to 600 °C at a ramp rate of 10 °C/min with an air flow rate of 20 mL/min using Shimadzu DRG-60.

Electrochemical Measurements. The electrochemical measurements were performed using two-electrode Swagelok-type cells (X2 Labwares, Singapore) with lithium serving as both the counter and reference electrodes under ambient temperature. The working electrode was composed of 70 wt % of active material (e.g., Co_3O_4 with different morphologies), 20 wt % of conductivity agent (carbon black, Super−P-Li), and 10 wt % of binder (polyvinylidenedifluoride, PVDF, Aldrich). The electrolyte used was 1.0 M $LiPF_6$ in a 50:50 (w/w) mixture of ethylene carbonate and diethyl carbonate. Cell assembly was carried out in an argon-filled glovebox with both moisture and oxygen contents below 1.0 ppm. Galvanostatic charging/discharging was performed using a battery tester (NEWAER) between 10 mV to 3 V at current rates of 50 and 100 mA g^{-1}.

REFERENCES AND NOTES

(1) Poizot, P.; Laruelle, S.; Grugeon, S.; Dupont, L.; Tarascon, J. M. *Nature* **2000**, *407* (6803), 496−499.
(2) Nam, K. T.; Kim, D. W.; Yoo, P. J.; Chiang, C. Y.; Meethong, N.; Hammond, P. T.; Chiang, Y. M.; Belcher, A. M. *Science* **2006**, *312* (5775), 885−888.
(3) Lou, X. W.; Deng, D.; Lee, J. Y.; Feng, J.; Archer, L. A. *Adv. Mater.* **2008**, *20*, 258−262.
(4) Xie, X.; Li, Y.; Liu, Z.-Q.; Haruta, M.; Shen, W. *Nature* **2009**, *458* (7239), 746−749.
(5) Hu, L.; Peng, Q.; Li, Y. *J. Am. Chem. Soc.* **2008**, *130* (48), 16136−16137.
(6) Cao, A. M.; Hu, J. S.; Liang, H. P.; Song, W. G.; Wan, L. J.; He, X. L.; Gao, X. G.; Xia, S. H. *J. Phys. Chem. B* **2006**, *110* (32), 15858−15863.
(7) Huang, F.; Yuan, Z. Y.; Zhan, H.; Zhou, Y. H.; Sun, J. T. *Mater. Lett.* **2003**, *57* (22−23), 3341−3345.
(8) Kang, Y. M.; Song, M. S.; Kim, J. H.; Kim, H. S.; Park, M. S.; Lee, J. Y.; Liu, H. K.; Dou, S. X. *Electrochem. Acta* **2005**, *50* (18), 3667−3673.
(9) Larcher, D.; Sudant, G.; Leriche, J. B.; Chabre, Y.; Tarascon, J. M. *J. Electrochem. Soc.* **2002**, *149* (3), A234−A241.
(10) Li, W. Y.; Xu, L. N.; Chen, J. *Adv. Funct. Mater.* **2005**, *15* (5), 851−857.
(11) Li, Y. G.; Tan, B.; Wu, Y. Y. *Nano Lett.* **2008**, *8* (1), 265−270.
(12) Shaju, K. M.; Jiao, F.; Debart, A.; Bruce, P. G. *Phy. Chem. Chem. Phy.* **2007**, *9* (15), 1837−1842.
(13) Xie, X. W.; Shen, W. J. *Nanoscale* **2009**, *1* (1), 50−60.
(14) Wang, X.; Chen, X. Y.; Gao, L. S.; Zheng, H. G.; Zhang, Z.; Qian, Y. T. *J. Phys. Chem. B* **2004**, *108* (42), 16401−16404.
(15) Li, C. C.; Yin, X. M.; Wang, T. H.; Zeng, H. C. *Chem. Mater.* **2009**, *21* (20), 4984−4992.
(16) Zhu, T.; Chen, J. S.; Lou, X. W. *J. Mater. Chem.* **2010**, *20*, 7015−7020.
(17) Lou, X. W.; Deng, D.; Lee, J. Y.; Archer, L. A. *J. Mater. Chem.* **2008**, *18* (37), 4397−4401.
(18) Cao, L.; Xu, F.; Liang, Y. Y.; Li, H. L. *Adv. Mater.* **2004**, *16* (20), 1853−1857.
(19) Zhou, W. J.; Zhang, J.; Xue, T.; Zhao, D. D.; Li, H. L. *J. Mater. Chem.* **2008**, *18* (8), 905−910.
(20) Needham, S. A.; Wang, G. X.; Konstantinov, K.; Tournayre, Y.; Lao, Z.; Liu, H. K. *Electrochem. Solid State Lett.* **2006**, *9* (7), A315−A319.
(21) Wu, Z.-S.; Ren, W.; Wen, L.; Gao, L.; Zhao, J.; Chen, Z.; Zhou, G.; Li, F.; Cheng, H.-M., *ACS Nano* **2010**.
(22) He, T.; Chen, D. R.; Jiao, X. L.; Wang, Y. L.; Duan, Y. Z. *Chem. Mater.* **2005**, *17* (15), 4023−4030.
(23) Li, Y. G.; Tan, B.; Wu, Y. Y. *J. Am. Chem. Soc.* **2006**, *128* (44), 14258−14259.
(24) Salabas, E. L.; Rumplecker, A.; Kleitz, F.; Radu, F.; Schuth, F. *Nano Lett.* **2006**, *6* (12), 2977−2981.
(25) Keng, P. Y.; Kim, B. Y.; Shim, I.-B.; Sahoo, R.; Veneman, P. E.; Armstrong, N. R.; Yoo, H.; Pemberton, J. E.; Bull, M. M.; Griebel, J. J.; Ratcliff, E. L.; Nebesny, K. G.; Pyun, J. *ACS Nano* **2009**, *3* (10), 3143−3157.
(26) Ryu, J.; Kim, S.-W.; Kang, K.; Park, C. B. *ACS Nano* **2009**, *4* (1), 159−164.
(27) Xu, R.; Zeng, H. C. *J. Phys. Chem. B* **2003**, *107* (46), 12643−12649.
(28) Lou, X. W.; Deng, D.; Lee, J. Y.; Feng, J.; Archer, L. A. *Adv. Mater.* **2008**, *20* (2), 258−262.
(29) Shi, X. Y.; Han, S. B.; Sanedrin, R. J.; Galvez, C.; Ho, D. G.; Hernandez, B.; Zhou, F. M.; Selke, M. *Nano Lett.* **2002**, *2* (4), 289−293.
(30) Hou, Y. L.; Kondoh, H.; Shimojo, M.; Kogure, T.; Ohta, T. *J. Phys. Chem. B* **2005**, *109* (41), 19094−19098.
(31) Liu, X. H.; Yi, R.; Zhang, N.; Shi, R. R.; Li, X. G.; Qiu, G. Z. *Chem. Asian J.* **2008**, *3* (4), 732−738.
(32) Liu, Z. P.; Ma, R. Z.; Osada, M.; Takada, K.; Sasaki, T. *J. Am. Chem. Soc.* **2005**, *127* (40), 13869−13874.
(33) Sampanthar, J. T.; Zeng, H. C. *J. Am. Chem. Soc.* **2002**, *124* (23), 6668−6675.
(34) Figlarz, M.; Guenot, J.; Fievetvincent, F. *J. Mater. Sci.* **1976**, *11* (12), 2267−2270.
(35) Feng, J.; Zeng, H. C. *Chem. Mater.* **2003**, *15* (14), 2829−2835.
(36) Liu, X. H.; Qiu, G. Z.; Li, X. G. *Nanotechnology* **2005**, *16* (12), 3035−3040.
(37) Xu, R.; Zeng, H. C. *J. Phys. Chem. B* **2003**, *107* (4), 926−930.
(38) Yang, L. X.; Zhu, Y. J.; Li, L.; Zhang, L.; Tong, H.; Wang, W. W.; Cheng, G. F.; Zhu, J. F. *Eur. J. Inorg. Chem.* **2006**, (23), 4787−4792.
(39) Cong, H. P.; Yu, S. H. *Cryst. Growth Des.* **2009**, *9* (1), 210−217.
(40) Yu, T.; Zhu, Y. W.; Xu, X. J.; Shen, Z. X.; Chen, P.; Lim, C. T.; Thong, J. T. L.; Sow, C. H. *Adv. Mater.* **2005**, *17* (13), 1595−1599.
(41) Varghese, B.; Hoong, T. C.; Yanwu, Z.; Reddy, M. V.; Chowdari, B. V. R.; Wee, A. T. S.; Vincent, T. B. C.; Lim, C. T.; Sow, C. H. *Adv. Funct. Mater.* **2007**, *17* (12), 1932−1939.
(42) Fu, L.; Liu, Z. M.; Liu, Y. Q.; Han, B. X.; Hu, P. G.; Cao, L. C.; Zhu, D. B. *Adv. Mater.* **2005**, *17* (2), 217−221.

(43) Wang, X.; Yu, L. J.; Wu, X. L.; Yuan, F. L.; Guo, Y. G.; Ma, Y.; Yao, J. N. A. *J. Phys. Chem. C* **2009**, *113* (35), 15553–15558.

(44) Xu, R.; Zeng, H. C. *Langmuir* **2004**, *20* (22), 9780–9790.

(45) Sugimoto, T.; Matijevic, E. *J. Inorg. Nucl. Chem.* **1979**, *41* (2), 165–172.

(46) David, W. I. F.; Thackeray, M. M.; Bruce, P. G.; Goodenough, J. B. *Mater. Res. Bull.* **1984**, *19* (1), 99–106.

(47) Poizot, P.; Laruelle, S.; Grugeon, S.; Dupont, L.; Tarascon, J. M. *J. Power Sources* **2001**, *97−8*, 235–239.

(48) Yuan, Z. Y.; Huang, F.; Feng, C. Q.; Sun, J. T.; Zhou, Y. H. *Mater. Chem. Phys.* **2003**, *79* (1), 1–4.

(49) Fu, Z. W.; Wang, Y.; Zhang, Y.; Qin, Q. Z. *Solid State Ionics* **2004**, *170* (1−2), 105–109.

(50) Lu, Y.; Wang, Y.; Zou, Y. Q.; Jiao, Z.; Zhao, B.; He, Y. Q.; Wu, M. H. *Electrochem. Commun.* **2010**, *12* (1), 101–105.

(51) Rahman, M. M.; Wang, J. Z.; Deng, X. L.; Li, Y.; Liu, H. K. *Electrochem. Acta* **2009**, *55* (2), 504–510.

(52) Wang, Y.; Xia, H.; Lu, L.; Lin, J. *ACS Nano* **2010**, *4* (3), 1425–1432.

(53) Barreca, D.; Cruz-Yusta, M.; Gasparotto, A.; Maccato, C.; Morales, J.; Pozza, A.; Sada, C.; Sainchez, L.; Tondello, E. *J. Phys. Chem. C* **2010**, *114* (21), 10054–10060.

(54) Liu, J.; Cao, G. Z.; Yang, Z. G.; Wang, D. H.; Dubois, D.; Zhou, X. D.; Graff, G. L.; Pederson, L. R.; Zhang, J. G. *ChemSusChem* **2008**, *1* (8−9), 676–697.

(55) Chen, J. S.; Li, C. M.; Zhou, W. W.; Yan, Q. Y.; Archer, L. A.; Lou, X. W. *Nanoscale* **2009**, *1*, 280–285.

(56) Chakroune, N.; Viau, G.; Ammar, S.; Jouini, N.; Gredin, P.; Vaulay, M. J.; Fievet, F. *New J. Chem.* **2005**, *29* (2), 355–361.

(57) Kruk, M.; Jaroniec, M. *Chem. Mater.* **2001**, *13* (10), 3169–3183.

(58) Lou, X. W.; Deng, D.; Lee, J. Y.; Archer, L. A. *Chem. Mater.* **2008**, *20*, 6562–6566.

(59) Tian, L.; Zou, H.; Fu, J.; Yang, X.; Wang, Y.; Guo, H.; Fu, X.; Liang, C.; Wu, M.; Shen, P. K.; Gao, Q. *Adv. Funct. Mater.* , *20* (4), 617–623.

(60) Chen, J. S.; Tan, Y. L.; Li, C. M.; Cheah, Y. L.; Luan, D.; Madhavi, S.; Boey, F. Y. C.; Archer, L. A.; Lou, X. W. *J. Am. Chem. Soc.* **2010**, *132* (17), 6124–6130.